Development updates for a two-dimensional axisymmetric hybrid code for Plasma Thruster discharges

IEPC-2017-201

Presented at the 35th International Electric Propulsion Conference
Georgia Institute of Technology – Atlanta, Georgia – USA
October 8–12, 2017

Daniel Pérez-Grande*, Jiewei Zhou† and Adrián Domínguez‡

and

Pablo Fajardo§ and Eduardo Ahedo¶

Aerospace Engineering, Universidad Carlos III de Madrid, Leganés, Madrid, 28911, Spain

The manuscript presents development updates on a new new two-dimensional, axisymmetric, hybrid particle-fluid code for simulation of plasma discharges, particularly, in Hall Effect thrusters. The overall code structure and main design rationale are introduced; particularities for the particle segment are commented, including the algorithms for particle-surface interaction and the kinetic Bohm correction. The macroscopic fluid model for the electron population, based on a bi-Maxwellian, two temperature approximation, and its resolution are described; an update is provided on the spatial gradient reconstruction approach used throughout the model. Finally, preliminary results for a well known Hall Effect Thruster are provided, both for a typical radial magnetic topography and for a version which includes a singular point within the simulation domain.

I. Introduction

The Electric Propulsion (EP) landscape is rapidly evolving: next generation thrusters belonging to proven technologies, such as the the Hall-Effect Thruster (HET), are being designed for larger on-board available power, different control schemes and new mission scenarios, ranging from Planetary Exploration to traditional station keeping; indeed, HETs are currently the main technological solution for near-earth EP, with the exception of micro-EP.

Electric propulsion technologies currently enjoy dedicated development efforts as part of an effort to improve European competitiveness in Space; particularly, as part of the Horizon2020 framework (specifically, the EPIC project). Included in said framework is the development of simulation tools that will allow for accurately modeling plasma discharges in a variety of different EP thrusters is an essential step in order to reduce development time and costs, reveal optimization opportunities and predict operational parameters throughout the thrusters lifetime.

In this line, the EP2 group is currently developing NOMADS (Non-structured Magnetically Aligned Discharge Simulator) a HET simulation platform. The code is based on the group's expertise with previous simulation codes such as HallMA[1] and HPHall2, hybrid codes for HET simulations based on the original

*PhD candidate, Aerospace Engineering (Universidad Carlos III de Madrid), daperezg@ing.uc3m.es
†PhD candidate, Aerospace Engineering (Universidad Carlos III de Madrid), jiewei.zhou@uc3m.es
‡PhD candidate, Aerospace Engineering (Universidad Carlos III de Madrid), addoming@ing.uc3m.es
§Associate Professor, Aerospace Engineering (Universidad Carlos III de Madrid), pfajardo@ing.uc3m.es
¶Professor, Aerospace Engineering (Universidad Carlos III de Madrid), eahedo@ing.uc3m.es

HPHall by Fife.[2] NOMADS is built with much of the heritage of previous codes in mind but with the intention of expanding their functionality to provide a more flexible and capable environment.

NOMADS is a hybrid Particle In Cell (PIC) and macroscopic fluid code purposed for solving an axisymmetric description of the plasma in the thruster and near-plume regions. It is able to model low density, low collisionality plasmas, with strong magnetization of the electron population and negligible self-field production and ion magnetization. In principle, while current focus is on HETs, the conditions modeled include various other electromagnetic-type thrusters, which could be part of the scope of the tool in the future.

This manuscript presents an update on the current development status of NOMADS. Section II provides an overview of the overall segments, numerical model and methods implemented in the code, with some particularities and resolution description. Section III provides some preliminary results for simulations of the SPT-100 HET, including a version of the thruster in which a singular point has been introduced next to the anode region.

II. Numerical model

A. Overall structure and main simulation loop

The code overall arquitecture and structure is based on modularity making use of Open MP for parallelization and HDF5 for data management.[3] As a hybrid PIC-fluid simulator, two central modules participate in the main simulation loop: the PIC module, in charge of propagating the heavy species (ions and neutrals macro-particles) one time step forward using the electric potential and the electron temperature fields, obtaining the plasma density and particle fluxes. Secondly, the electron-fluid module takes ion currents and plasma density (assuming quasineutrality), as well as neutral density, and solves an electron fluid model, updating the electric potential and the electron temperature, thus closing the loop. The fluid model utilizes various Boundary Conditions (BC); amongst them, a sheath model for the plasma-wall interaction has been implemented (see Section II.C). Figure 1 shows a summary of the computational loop in NOMADS.

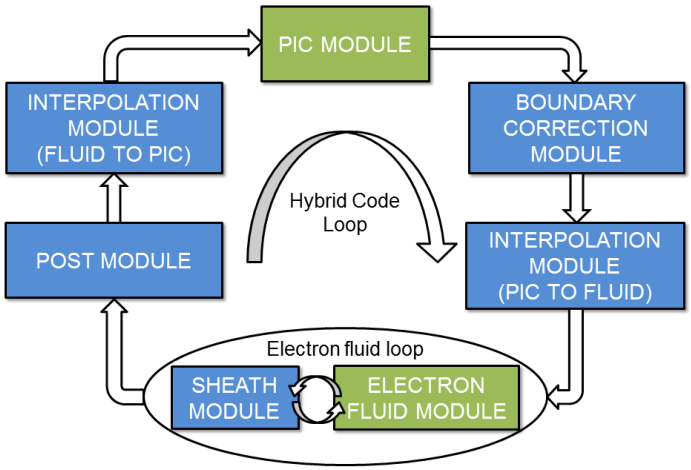

Figure 1. Hybrid particle-fluid computational loop

B. The heavy species PIC module

The main characteristics including most of the PIC module algorithms are already described in detail in Refs. 3, 4. PIC innovations in the treatment of the heavy species are focused on improving the statistics. Dedicated computational lists storing all necessary particle related information are considered for the various ion and neutral macro-particles populations (such as singly and doubly charged ions and injected neutrals). A dedicated particle-list-wise population control maintains, for each heavy species the number of macro-particles per cell within a given specified range, thus reducing PIC associated noise in the macroscopic magnitudes obtained at the PIC mesh nodes through the particle weighting algorithms, while limiting the

computational time spent in this segment of the algorithm. A PIC mesh cell wise particle collider algorithm carries out the ionization collisional processes up to second degree using Drawin model[5] (for reactions $A+e \rightarrow A^+ + 2e$ and $A + e \rightarrow A^{++} + 3e$) and Bell model[6] (for $A^+ + e \rightarrow A^{++} + 2e$) following an approach similar to that of HPHall.[2] The surface interaction and the Kinetic Bohm condition forcing algorithm are described next.

1. *Particle-surface interaction*

The structured PIC mesh allows the identification of every PIC mesh surface (segment connecting two PIC mesh nodes) with a set of 2 indices. Thus, a 2D surface element matrix is defined storing an integer value indicating the type of each surface element.[3] The basic surface element types and their effects on ion and neutral macro-particles are listed on Table 1. The same PIC mesh containing the axis $r = 0$ is used in all the simulations performed in this work, and is depicted in Fig. 2. It is worth to note that the axis $r = 0$ is transparent for the particles, which naturally suffer a specular reflection there.

Surface type	**Effects on ions**	**Effects on neutrals**
Transparent	None	None
Free loss	Removal	Removal
Injection	Stochastic injection	Stochastic injection
Material wall	Recombination	Reflection

Table 1. PIC mesh surface elements types and corresponding effects on macro-particles.

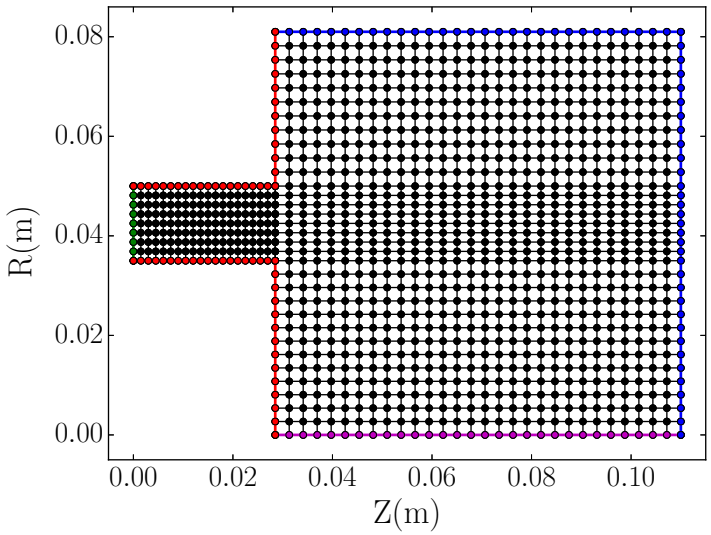

Figure 2. PIC mesh considered for all the simulations. The purple line and nodes correspond to the axis $r = 0$. Green, red and blue nodes refer to injection, material wall and free loss boundaries, respectively.

All macro-particles crossing a boundary surface element (non-transparent) are considered for the surface interaction algorithm, which updates the macroscopic magnitudes on the surface elements through a surface weighting algorithm and carries out the corresponding effects depending on both the macro-particle and the surface type according to Table 1. A zeroth-order extended surface weighting scheme[7,8] is implemented providing more accurate macroscopic magnitudes at boundary nodes. At a given time step k, simple surface weighted particle density and flux vector are obtained at the central point of every material surface element as

$$n_{sw}^{(k)} = \frac{1}{\Delta t \Delta S} \sum_{p=1}^{N_{hit}} \frac{W_p}{v_{\perp,p}} \tag{1}$$

$$\vec{g}_{sw}^{(k)} = \frac{1}{\Delta t \Delta S} \sum_{p=1}^{N_{hit}} \frac{W_p \vec{v}_p}{v_{\perp,p}} \tag{2}$$

where N_{hit} is the number of hitting macro-particles on each surface element of area ΔS, being $v_{\perp,p}$ the macro-particle perpendicular velocity to the surface and W_p and $\vec{v}_p$ its corresponding macro-particle weight and velocity vector. The extended time-averaged associated quantities allow for noise reduction due to the typical low number of particles crossing a boundary face on simulation time steps. The time-averaged surface weighted density is computed as

$$\overline{n}_{sw}^{(k)} = \frac{(\Delta k_{avg} - 1)\overline{n}_{sw}^{(k-1)} + n_{sw}^{(k)}}{\Delta k_{avg}} \tag{3}$$

with Δk_{avg} the averaging number of time steps and k and $k-1$ referring to two consecutive time steps; typical recommended values for the averaging number are between $50-100$.[8] This scheme is applied similarly for all surface weighted magnitudes computed, which are finally interpolated from the surface elements to the corresponding boundary nodes.

After performing the surface weighting process, hitting ion macro-particles on material boundaries are recombined into neutrals to be re-injected in the domain while every neutral macro-particle suffers either a diffuse or specular reflection. This last reflection is carried out by simply inverting the particle normal velocity component to the corresponding surface element. On the other hand, a thermal Maxwellian emission from the surface is considered for the neutral re-injection due to either ion recombination process or diffuse reflection. The re-injection probability distribution function is

$$f_{reinj}(\vec{v}) \propto v_\perp \exp\left(-\frac{m|\vec{v}|^2}{2T_{reinj}}\right) \tag{4}$$

where the re-injection temperature is obtained as $2T_{reinj} = \overline{E}_{reinj}$ with

$$\overline{E}_{reinj} = \alpha_W 2T_W + (1 - \alpha_W)\overline{E}_{imp} \tag{5}$$

the mean re-injection energy. The wall accommodation coefficient, α_W modulates the two contributions to this mean energy: a wall contribution through a wall temperature T_W (in energy units) and the time-averaged total impacting energy of the hitting population (per elementary particle) $\overline{E}_{imp}$. In case of ion macro-particles, the sheath potential fall $\Delta\phi_{sh}$ is taken into account in the impacting energy (per elementary particle) so that

$$E_{imp} = E_k + eZ\Delta\phi_{sh} \tag{6}$$

being E_k the kinetic energy per elementary particle.

2. The Bohm correction

Due to the different mobilities of electrons and ions in a quasineutral plasma, an ion-attracting sheath with extension of several Debye lengths develops at the boundary between the plasma and a given absorbing boundary wall.[9,10] In typical cases (those considered in the hybrid simulator), the sheath is quasiplanar, quasisteady, collisionless and unmagnetized. If ϕ_S and ϕ_W are the electric potential at sheath edge and wall, respectively, for the stable existance of such sheath with $\Delta\phi_{sh} = \phi_S - \phi_W > 0$, the ions must satisfy the *kinetic* Bohm condition at the sheath edge[7,8]

$$\sum_{s=1}^{L} \int_0^\infty \left(\frac{Z_s}{T_e} - \frac{Z_s^2}{m_s v_\perp^2}\right) f_s(v_\perp) dv_\perp \geq 0, \tag{7}$$

where L is the total number of ion populations and m_s, Z_s and f_s are the mass, charge number and distribution function at the sheath edge (integrated over parallel velocities) of the s^{th} ion population, respectively. Using the surface weighting scheme, the equivalent PIC version of that condition is

$$P \equiv \frac{1}{\Delta t \Delta S} \sum_{s=1}^{L} \sum_{p=1}^{N_{hit}} \left(\frac{Z_s}{T_e} - \frac{Z_s^2}{m_s v_{\perp,p}^2} \right) \frac{W_p}{v_{\perp,p}} > 0 \tag{8}$$

The kinetic Bohm condition forcing algorithm[8] evaluates Eq. (8) on every PIC mesh surface element. Whenever $P < 0$ an additional potential fall $\delta\phi$ corresponding to a Bohm correction forcing layer is imposed so that the plasma density is reduced accordingly in order to adapt the electric potential and satisfy Bohm condition ($P \approx 0$) increasing the ion perpendicular velocity to the wall. As shown in Ref. 8, this $\delta\phi$ tends to zero in stationary conditions.

C. The electron fluid module

NOMADS revieves its name from the electron fluid module which has been implemented; this model responds to the assumption that the magnetized electron population may be treated as fluid, similarly to how HallMa[1] or Hall2De[11] approach the subject. In particular, two of the major assumptions in the former code have been forgone:

- The description of the electron fluid is quasi-1D: magnetic field lines are characterized by constant temperature and a constant "thermalized" potential solution.
- The Electron Velocity Distribution Function (EVDF) follows a Maxwellian description with isotropic electron temperature.

The first implies that NOMADS solves a fully 2D-axisymmetric problem, instead of the 1D problem initially proposed by Fife.[2] This does not imply, however, that the "isothermal" property of magnetic field lines, typical in HETs, is not recovered in the 2D solution, but that, by discretizing to a 2D Magnetic Field Aligned Mesh (MFAM) it is possible to consider a simulation domain that is not only limited to an assortment of magnetic flux "tubes" (as in the 1D problem), but that may include more complex magnetic topographies (e.g. singular points) and boundary descriptions. The use of the MFAM was justified for an anisotropic medium such as the magnetized electron fluid in Ref. 12, where the added complexity of mesh generation and Gradient Reconstruction (GR) for this type of mesh was also explored. An update into the subject of GR, particularly when using the Weighted Least Squares Face Interpolation (WLSQRFI) method proposed by Sozer[13] is given in Section II.D.

The MFAM represents a simulation domain split into toroidal volume elements, where each of the faces is closely aligned with one the local directions defined by the magnetic field. Figure 3 shows a particular magnetic topography and associated MFAM: *blue faces* represent lines of constant magnetic stream function and follow the local parallel direction to the magnetic field, $\vec{1_{\parallel}}$; *red faces* represent lines of constant magnetic scalar potential, and are aligned with the local perpendicular-to-the-magnetic-field direction in the Z-R plane, $\vec{1_{\top}}$. The azimuth direction, $\vec{1_{\theta}}$, perpendicular to the Z-R plane, completes the magnetic reference system and, alongside $\vec{1_{\top}}$ defines the plane in which the "perpendicular" macroscopic characteristics for the electron fluid are obtained; for example, in the case of fluid temperatures, the relevant variables are defined as follows:

$$\begin{gathered} T_{e\parallel} = \frac{m_e}{k_B} \left\langle c_{e\parallel}^2 \right\rangle \;\; ; \quad T_{e\perp} = \frac{m_e}{2k_B} \langle c_{e\perp}^2 \rangle = \frac{m_e}{2k_B} \langle c_{e\top}^2 + c_{e\theta}^2 \rangle \,, \\ T_e = \frac{T_{e\parallel} + 2T_{e\perp}}{3} \end{gathered} \tag{9}$$

where c_e is the electron velocity.

The problem is poised to be solved through the Finite Volume Method (FVM), applied to each of the annular volumes exemplified in Fig. 3, differentiating between equations applicable to either the parallel or perpendicular directions to the magnetic field.

Regarding the EVDF, a bi-Maxwellian description is employed, with two distinct electron temperatures related, again, to the magnetic field directions:

$$f_e = \frac{n_e}{(2\pi)^{3/2}} \left(\frac{m_e}{k_B T_{e\parallel}} \right)^{1/2} \frac{m_e}{k_B T_{e\perp}} \exp\left(-\frac{1}{2} \frac{m_e}{k_B T_{e\perp}} c_{e,\perp}^2 - \frac{1}{2} \frac{m_e}{k_B T_{e\parallel}} c_{e,\parallel}^2 \right), \tag{10}$$

where the electron drift, or bulk, velocity, $\vec{u}_e$, has been neglected versus the particle velocity, $\vec{c}_e$. Barakat & Schunk[14] use this description to take moments of the Boltzmann equation, leading to a 16 moment approximation of the fluid.

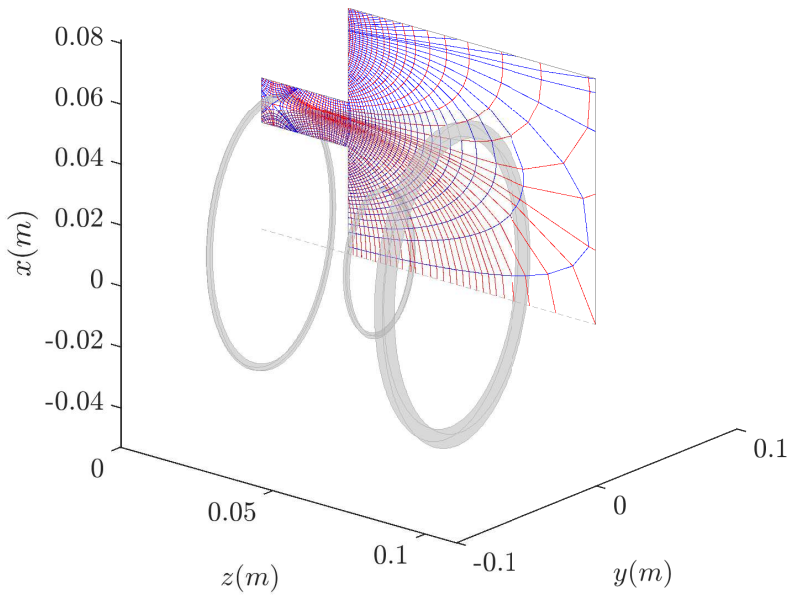

Figure 3. 2D-axisymmetric Magnetic Field Aligned Mesh and Volume elements

The rationale for this change is related with the scope of possible future applications for NOMADS, in which thrusters that present magnetic nozzles could be simulated. In this type of magnetic topographies an anisotropic description of the electron population is necessary; it is also reasonable to argue that the anisotropy imposed by the magnetic field carries over to the population description itself. The model used is a reduced version of Barakat & Schunk's model, applying the following assumptions:

- The plasma is quasi-neutral for the scales considered within the simulation domain.
- Electron drift kinetic energy may be neglected with respect to electron thermal energy.
- Neutral population drift velocities are neglected.
- Viscous terms are neglected: the model is reduced to a 12 moment approximation.
- Convective and non-stationary terms in the momentum and heat-flow equations will be neglected with respect to electron pressure terms; thus, these equations become "state" equations which only depend on the time evolution of the problem implicitly, through the electron temperature and plasma density.
- The collisional terms for the momentum and energy equations will be modeled using Maxwell-type molecule interactions.
- The model is closed by using the Fourier type Krook's relaxation model for the collisional terms in the heat-flow equations.

- Azimuthal terms in the equations, which in HETs are suspected to be responsible for non-classical electron transport, are substituted by the well known "anomalous collisionality", which enters the equations as a factor of the electron gyro-frequency:

$$\nu_{anomalous} = \alpha_{anomalous}\Omega_{ce} \tag{11}$$

  Other known non-classical terms such as the "wall collisionality" are neglected at the present moment, following the rationale given by Hofer,[15] by which typical values of the anomalous collisionality are, at least, an order of magnitude larger than other non-classical terms.

NOMADS integrates three equations in the control volumes of the simulation domain: a generalized Ohm's law, based on the current continuity and momentum equations, the Thermal Energy Density equation and the Parallel Internal Energy equation; the latter solve for the total and parallel electron pressure, p_e and $p_{e\|}$, respectively, and the electron density is obtained from the PIC segment. The generalized Ohm's law for the *ith* control volume in the simulation domain, E, i, derives from the total current continuity equation and may be solved, in typical FVM fashion, by applying Gauss and approximating integrals over the area of the *jth* face, F, j, of an element volume:

$$\begin{gathered}\iint\limits_{V_{E,i}} \nabla\cdot(\vec{j}_e+\vec{j}_i)dV = \iint\limits_{V_{E,i}} I_d\cdot dV \rightarrow \\ \rightarrow \oiint\limits_{A_{F,j(E,i)}} (\vec{j}_e+\vec{j}_i)\cdot\vec{n}dA \approx \left(\sum_j \left(j_{e\top}\vec{1}_\top + j_{e\theta}\vec{1}_\theta + j_{e\|}\vec{1}_\| + \vec{j}_i\right)\Big|_{F,j}\vec{n}_{F,j}A_{F,j}\right)\Bigg|_{E,i} \approx I_{d,E,i}\cdot V_{E,i}\end{gathered} \tag{12}$$

The term $I_{d,V_{E,i}}$ represents the possibility of current being externally injected into the domain, simulating, for example, the presence of a HET hollow cathode; typically this variable is 0 for most of the simulation domain. For further clarity, typical simulation volumes are shown in next:

The electron currents are obtained from the momentum equation in Ref. 14 and, together with the previous assumptions may be written as:

$$\begin{gathered}\vec{1}_\top : j_{e\top}|_{F,j} = \frac{1}{\eta_{e^*}(1+(\beta_{e^*})^2)}\Bigg|_{F,j}\left(-\nabla_\top\phi + \frac{1}{2en_e}\nabla_\top\left(3p_e - p_{e\|}\right) - \frac{3(p_e-p_{e\|})}{2en_eB}\nabla_\top B - \right. \\ \left. - \sum_{Z=1}^{2,3,\ldots}\eta_{ei_Z}j_{i_Z\top}\right)\Bigg|_{F,j} \\ \vec{1}_{\boldsymbol{\theta}} : j_{e\theta}|_{F_j} = \beta_{e^*}j_{e\top}|_{F_j} \\ \vec{1}_\| : j_{e\|}\big|_{F,j} = \frac{1}{\eta_e}\Bigg|_{F,j}\left(-\nabla_\|\phi + \frac{1}{en_e}\nabla_\|p_{e\|} + \frac{3(p_{e\|}-p_e)}{2en_eB}\nabla_\|B - \sum_{Z=1}^{2,3,\ldots}\eta_{ei_Z}j_{i_Z\|}\right)\Bigg|_{F,j}\end{gathered} \tag{13}$$

Electron pressures and temperatures are related through the gas state law:

$$p_e = n_ek_BT_e \; ; \; p_{e\|} = n_ek_BT_{e\|} \tag{14}$$

Electron-to-ion resistivities, η_{ei_Z}, depend on the elastic collision frequency between both populations, ν_{ei_Z}; the *effective* electron resistivity, η_{e^*}, depends on all of the collisional frequencies pertaining electrons: electron-to-heavy-species elastic and inelastic (ionization, excitation and recombination) collisions and the anomalous collisionality; the hall parameter relates the gyro-frequency and the effective electron collisional frequency, ν_{e^*}:

$$\beta_{e^*} = \frac{\frac{eB}{m_e}}{\nu_{e^*}} = \frac{\Omega_{ce}}{\nu_{e^*}}; \quad \eta_{e^*} = \frac{m_e\nu_{e^*}}{e^2n_e}; \quad \eta_e = \frac{m_e\nu_e}{e^2n_e}$$

$$\nu_e = \nu_e = \nu_{en} + \sum_{Z=1}^{2,3,\ldots}\nu_{ei_Z} + (\nu_{ioniz.} - \nu_{recomb.}); \; \nu_{e^*} = \nu_e + \alpha_{anomalous}\Omega_{ce}$$

Equation 12 leads to a system of equations for the plasma potential at element centers, ϕ_{E_i}, when gradients are numerically discretized for face centers:

$$\{\boldsymbol{GR}\} \cdot \{\boldsymbol{\phi_E}\} = \{\boldsymbol{D}\} + \{\boldsymbol{P}\} + \{\boldsymbol{B}\} + \{\boldsymbol{I_{d,E}}\} \tag{15}$$

where $\{D\}$ represents the drag posed by the ion population (which is obtained from the PIC module), $\{P\}$ the effect due to electron pressure gradients, $\{B\}$ the effects of magnetic field non-uniformity and $\{I_{d,e}\}$ the current injection terms; $\{GR\}$ represents the resulting coefficients matrix associated to Gradient Reconstruction at faces in each element. This system of equations can be linearized together with appropriate Boundary Conditions (BC) and solved numerically; in particular, the PARDISO[16,17] direct solver for parallelized computation is used.

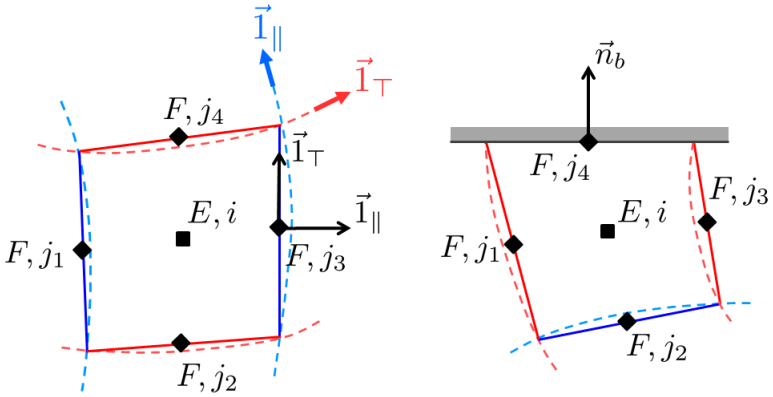

Figure 4. Examples of internal and boundary control volumes

The Thermal Energy Density and Parallel Internal Energy equations for a particular control volume and the faces that bound it are, after applying the aforementioned assumptions and the Gauss theorem:

$$\int_{V_{E,i}} \frac{3}{2}\frac{\partial p_e}{\partial t} dV - \oint_{A_{F,j}} \frac{3}{2en_e} p_e \cdot \vec{j}_e \cdot \vec{n} dA - \int_{V_{E,i}} B \left(\frac{3p_e - p_{e\parallel}}{2er} \nabla_\top \left(r j_{e\top} B^{-1} n_e^{-1} \right) + \right.$$
$$\left. + \frac{p_{e\parallel}}{e} \nabla_\parallel \left(j_{e\parallel} B^{-1} n_e^{-1} \right) \right) dV + \oint_{A_{F,j}} \vec{q}_e \cdot \vec{n} dA = \int_{V_{E,i}} \left(E_{coll} + \frac{\vec{j}_e}{en_e} \cdot \vec{M}_{coll} + \frac{|\vec{j}_e|^2}{2e^2 n_e^2} S_e m_e \right) dV$$

$$\int_{V_{e,i}} \frac{\partial p_{e\parallel}}{\partial t} dV - \oint_{A_{F,j}} \frac{p_{e\parallel}}{en_e} \cdot \vec{j}_e \cdot \vec{n} dA - \int_{V_{e,i}} B \frac{2p_{e\parallel}}{e} \nabla_\parallel \left(\frac{1}{B} \frac{j_{e\parallel}}{n_e} \right) dV + \tag{16}$$
$$\oint_{A_{F,j}} \vec{q}_e^{\,\parallel} \cdot \vec{n} dA - \int_{V_{e,i}} \frac{2}{B} \left[q_{e\top}^{\parallel} \nabla_\top B - \left(q_{e\parallel} - \frac{1}{2} q_{e\parallel}^{\parallel} \right) \nabla_\parallel B \right] dV =$$
$$\int_{V_{e,i}} \left(E_{coll\parallel} + 2\frac{j_{e\parallel}}{en_e} \cdot M_{coll\parallel} + \frac{j_{e\parallel}^2}{e^2 n_e^2} S_e m_e \right) dV$$

where E_{coll}, M_{coll} and S_e are, respectively, the collisional terms in the energy equation (inelastic and elastic terms), the collisional terms in the momentum equation (shown in Eq. (13) as the drag term) and the plasma production term; the heat-flow equations may be reduced from Ref. 14 and are not reproduced here for the sake of brevity.

Equations (16) are solved using a semi-implicit time-scheme, as in Ref. 11, in which terms that are explicit with electron pressure are solved implicitly, and terms that are implicit with it are solved explicitly; the use of this particular scheme was implemented after trials with fully explicit schemes, which required

time-step values for stability in the electron fluid equations that were too restrictive from the point of view of computational resources.

In order to exemplify the semi-implicit time-scheme, it may assumed that no anisotropy is present in the electron population, i.e. $T_e = T_{e,\parallel}$. In this case, the Thermal Energy Density and heat-flow equations are equivalent to the ones shown by Bittencourt:[18] the results shown in this manuscript also take into account this simplification. The discretization, approximating area and volume integrals in the same way as Eq. (12), results in a linear system of equations in the form:

$$\boldsymbol{\{p_{e,E}\}^{t+1} = \Delta t \left[\left(\{A\}^t + \{Ex\}^t \right) \cdot \{p_{e,E}\}^{t+1} + \{Q\}^t \cdot \{GR\} \cdot \{p_{e,E}\}^{t+1} + \{CS\}^t \right] + \{p_{e,E}\}^t} \tag{17}$$

where $\{A\}$ represents the electron current terms associated with advection, $\{Ex\}$ the terms associated with the gas expansion work, $\{Q\}$ the terms related with heat-flow (where only the gradient of pressure terms are treated implicitly) and $\{CS\}$ the collisional and source terms; note that each of the terms is evaluated at different times depending on if its treatment falls onto the implicit or explicit category, hence conferring the scheme its "semi-implicit" nature.

Finally, the electron fluid model is completed with ancillary models and BC:

The collisional rate and yield models for Xenon are as follows: elastic collisions were implemented based on the model proposed by Hayashi[19] for electron-neutral pairs and based on a Coulomb interaction model from Goldston[20] for electron-ion pairs. For the inelastic collisions, which suppose an energy sink in the electron fluid, Section II.B mentions the classic ionization reactions, to which the Hayashi[21] model for the excitation reaction $Xe^0 \rightarrow Xe^*$ is added. Recombination reactions are neglected.

The Plasma sheath model provides the boundary layer response derived from the interaction of the plasma and physical walls in the thruster; the sheath region resides *outside* of the simulation domain and is treated in NOMADS as a BC. The model implemented is based on the one presented by Ahedo and De Pablo;[22] it takes two distinct flavors depending on whether its applied to a non-floating-metallic or dielectric wall: in the first case (representing the anode wall in HETs), net current may exit the boundary and thus the sheath model takes the form:

$$\vec{j}_e \cdot \vec{n}_b \Big|_{F,j} = f_{sheath,metallic} \left(\Delta\phi_{sheath}, n_e, T_e \right) \; ; \; \Delta\phi_{sheath} = \phi_{F,j} - \phi_{wall} \tag{18}$$

where $\vec{n}_b$ is the vector normal-to-the-wall (Fig. 4); ϕ_{wall} is imposed and, in the case of the anode in HETs, becomes an operating condition for the thruster. The sheath model is linearized using a first order Taylor expansion of $\phi_{F,j}$, which may be reconstructed from $\{\phi_E\}$ through the WLSQRFI method, and comes into Eq. (15) by imposing the extracted electron current at the anode as the one allowed by the sheath. For a dielectric boundary (the ceramic walls typical in HETs), the BC becomes $(\vec{j}_e + \vec{j}_i)\Big|_{F,j} \cdot \vec{n}_b = 0$, since it may hold no net charge, and the sheath model takes the form:

$$\Delta\phi_{sheath}|_{F,j} = f_{sheath,dielectric} \left(\sum_{Z=1}^{2,3,\ldots} \vec{j}_{iZ} \cdot \vec{n}_b, n_e, T_e \right) \tag{19}$$

The heat deposited to the sheath by the plasma also depends on the type of wall and is also determined by the sheath model, providing a BC for the energy equations.

The exit BC is currently implemented as a non-homogeneous Neumann condition for $\nabla\phi$ and ∇p_e in the Ohm's law and energy equations by imposing $(\vec{j}_e + \vec{j}_i)\Big|_{F,j} \cdot \vec{n}_b = 0$ and $\vec{q}_e \cdot \vec{n}_b|_{F,j} = 0$

D. Updates on MFAM Gradient Reconstruction

GR is the process where the derivatives that appear in the discretized fluid equations are written in terms of the function values to be determined solving the fluid equations. These values are defined at the element's centers in the case of the MFAM used by NOMADS. In this case it is necessary to evaluate derivatives at the face's centers and element's centers. For a general function $\psi(x)$ its derivative at a certain point $\frac{d\psi}{dx}\Big|_i$ in terms of the its values at the surrounding element's centers ψ_j is:

$$\left.\frac{d\psi}{dx}\right|_i = \sum_j c_j \psi_j \tag{20}$$

Here i could refer to an element or face and x is a generic coordinate. The coefficients c_j are those to be determined via GR.

There is a previous work about GR on MFAMs carried out by our research group.[12] Until now the GR has been done using the WLSQRFI method introduced by Sozer.[13] This method is based on Taylor series expansions developed around the point where the derivatives are to be determined. Each expansion provides an equation and depending on its order there is a minimum number of ψ_j values required. Not only the first derivatives can be obtained but the derivatives of any order could be computed as well. Usually there are more equations than unknowns and a weighted least square process is conduced to solve the set of equations. When dealing with a non-structured mesh such as MFAMs this method is quite proper since it allows flexibility when choosing the order of the scheme and the values ψ_j to be used.

The GR can be done in different coordinate systems and the option that was implemented is based on magnetic coordinates, which constitute a orthogonal system defined by the magnetic field as:

$$\frac{\partial \lambda}{\partial r} = -rB_z, \ \frac{\partial \lambda}{\partial z} = rB_r \tag{21}$$

$$\frac{\partial \sigma}{\partial r} = B_r, \ \frac{\partial \sigma}{\partial z} = B_z \tag{22}$$

where r is the radial coordinate and z the axial coordinate of the cylindrical system. In the fluid equations the derivatives parallel and perpendicular to $\vec{B}$ are present and their relation with the magnetic coordinates are:

$$\nabla_{\parallel} \equiv B\frac{\partial}{\partial \sigma} \tag{23}$$

$$\nabla_{\top} \equiv rB\frac{\partial}{\partial \lambda} \tag{24}$$

One of the main problems of this approach is that there are singularities for the derivatives in magnetic coordinates near regions where the magnetic field is weak as seen in Eq. (23) and Eq. (24). Moreover, the derivative with respect to λ is not defined near the axis of symmetry either. As the magnetic coordinates are determined numerically small errors will be amplified near these singularities. Both regions of low magnetic field, for example singular points, and the case where the symmetry axis is considered are configurations of interest.

An alternative is to do the GR in cylindrical coordinates and then project the gradient vector into $\vec{1}_{\parallel}$ and $\vec{1}_{\top}$. The gradient in cylindrical coordinates is free of any singularities and it could get much more accurate results in regions of weak magnetic strength and near the symmetry axis.

In order to evaluate these approaches two tests have been conducted. In one of them the gradient reconstruction of the an analytic function is conducted and the numerical derivatives are compared with respect to the exact solution. This test is done for the SPT-100 HET with a magnetic topology given by Fig. 12. Regarding the second test the following equation is solved for this SPT-100 HET:

$$\nabla^2 \psi = p(r, z) \tag{25}$$

$$\frac{\partial \psi}{\partial \vec{n}_b} = h(r, z) \tag{26}$$

Here an analytic function is also used to obtain p and h. The integration of this problem is done through a FVM method. Thus, a previous GR is necessary and the results of the first test will be considered. In both of the tests the same linear function:

$$\psi(r, z) = r + z \tag{27}$$

is taken as trial function.

Figure 5 shows the results of the test for GR being (a) for magnetic coordinates and (b) for cylindrical system. In both of these subfigures there is a colormap illustrating the relative error of the numerical

derivatives. Furthermore, graphs about the statistics of those errors are represented as well. The WLSQFI scheme used is of first order and as the trial function is linear in cylindrical coordinates the approach followed in (b) is exact. However, the result obtained for this simple function in (a) is far from accurate in some locations. Unacceptable errors are present near the singular point and the symmetry axis. There are also large errors in other parts due to the low precision in the determination of the magnetic coordinates there. In the rest of the domain the errors are reasonable but still much worse compared with (b).

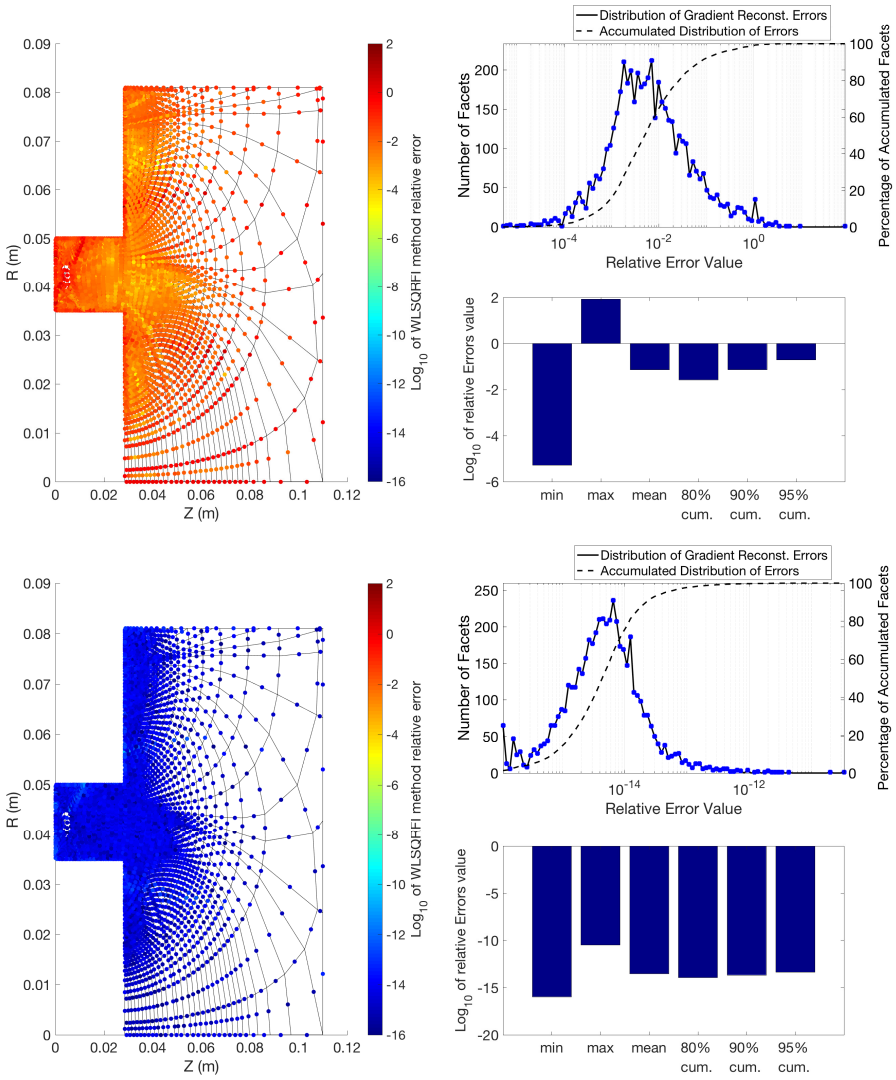

Figure 5. Gradient reconstruction test on an analytic function for (a) magnetic coordinates and (b) cylindrical coordinates.

Figure 6 presents the results for the integration test with (a) magnetic coordinates and (b) the cylindrical system. It is a completely analogous figure to Fig. 5 with colormaps about the relative error of the numerical solution and graphs regarding the statistics of those errors. Again here the approach in cylindrical coordinates is quite precise while it is observed in (a) that the errors of the GR have been spread over the domain. Although those inaccuracies in GR have affected the integration, it can be said that the trial function has been reconstructed in a reasonable way. This is since in 95% of the elements the relative error is within 7% and the maximum error is about 35%.

The above tests have been done for other trial functions as well getting similar results. Therefore, the GR in cylindrical coordinates is more robust than the approach followed up to now and it is to be implemented

soon. Then the magnetic coordinates gives unacceptable GR errors but they are localized, they do affect the integration of the equations afterwards but the it seems that the solution obtained is still reasonable.

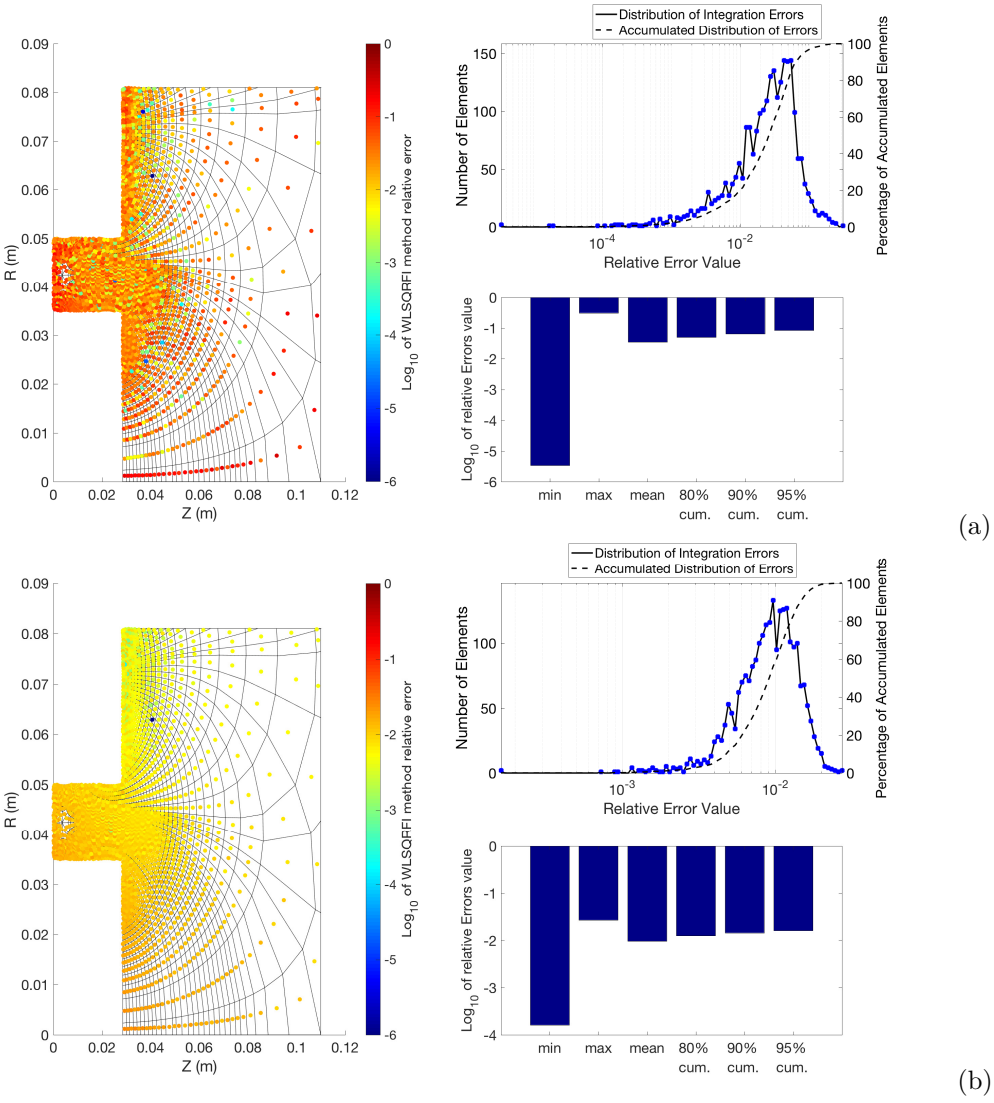

Figure 6. Integration test on an analytic function for (a) magnetic coordinates and (b) cylindrical coordinates.

III. Results

This section presents progress made on NOMADS related to full simulations of plasma thrusters; in particular, preliminary results for simulations of $500\mu s$ of operation are provided: both the SPT-100 HET with its base configuration for the magnetic topography and also for a configuration which includes a singular point within the simulation domain, achieved by locating a "trim magnet" behind the anode, have been simulated. Regarding the thruster walls, the sheath models correspond to BN ceramic walls, with the associated thermalization, Secondary Electron Emission (SEE) and electron backscatter parameters presented in Ref. 22; the anode wall presents a metallic conducting sheath with no SEE or backscattering.

The operational parameters for the simulations are:

PPU control	V_d	$\dot{m}$ (Xe)	PIC Δt	NOMADS Δt
Constant voltage	$300V$	$5\frac{mg}{s}$	$10^{-8}s$	$10^{-10}s$

Table 2. SPT-100 simulations operational parameters

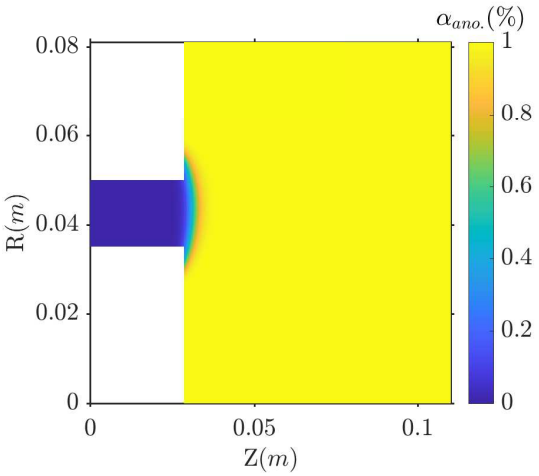

Figure 7. Anomalous collisionality factor

For the sake of comparison, the same spatial distribution of the $\alpha_{anomalous}$ parameter has been imposed in both simulations (Fig. 7); the implication is that the parameter has not been adjusted for the simulations to reproduce any particular operation point of the thruster. Two cases are analyzed:

A. SPT-100 base magnetic topography

The MFAM used for this simulation and the magnetic field in the simulation domain are shown in Fig. 8. As is expected, elements in the MFAM that are in regions of low magnetic field intensity, as in the last $50mm$ of the plume, are low in quality, with large faces that do not accurately represent the local directions of the magnetic field; further comment on this issue is made in Section IV. Note, however, that the simulation domain extends to the axis, $r = 0$, and up to $80mm$ downstream from the channel exit; this is a major difference from HallMa, in which simulation domains were typically smaller and could only be bounded by ceramic walls or magnetic field lines.

Some statistics for the simulation are presented in the following table:

No. PIC mesh elements	1080
Avg. No. macroparticles	$\sim 10^5$ Neutrals, $\sim 9\times10^4$ Single Ions, $\sim 9\times10^4$ Double Ions
No. MFAM elements	1326
No. cores	20
Computation time	$7.17\times10^4 s$: $4.6\times10^3 s$ in PIC, $6.6\times10^4 s$ in NOMADS

Table 3. Simulation statistics for "base" SPT-100 magnetic topography

The thruster is run in "constant voltage" mode and therefore the transient response of its operation may

be characterized through the discharge current; Fig. 9 demonstrates the characteristic "breathing mode" of HETs. Figure 10 presents some characteristic results for the plasma along the thruster channel center line.

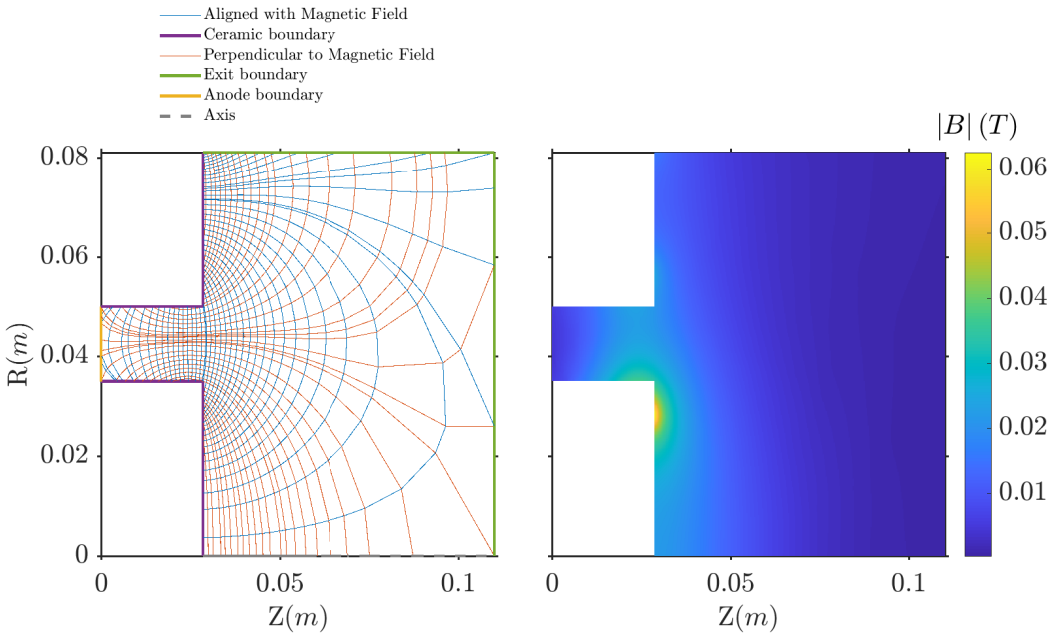

Figure 8. MFAM and Magnetic Field intensity in "base" SPT-100 magnetic topography; (A), (B) and (C) represent, respectively, time-steps of medium, high and low discharge current

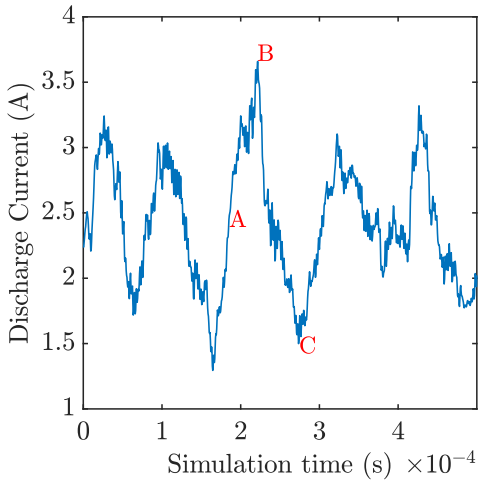

Figure 9. Discharge current in "base" SPT-100 magnetic topography

Additionally, time-averaged, 2D profiles of the simulation domain for some plasma variables are presented in Figure 11.

Note that the influence of the volumetric cathode (in which $\phi = 0$ is forced, according to the rationale for the constant voltage operation mode) may be seen both in Figs. 10 and 11. The order of magnitude of the remaining fluid variables is as expected; the instant results shown in Fig. 10 demonstrate the variable nature of the thruster's operation and profiles.

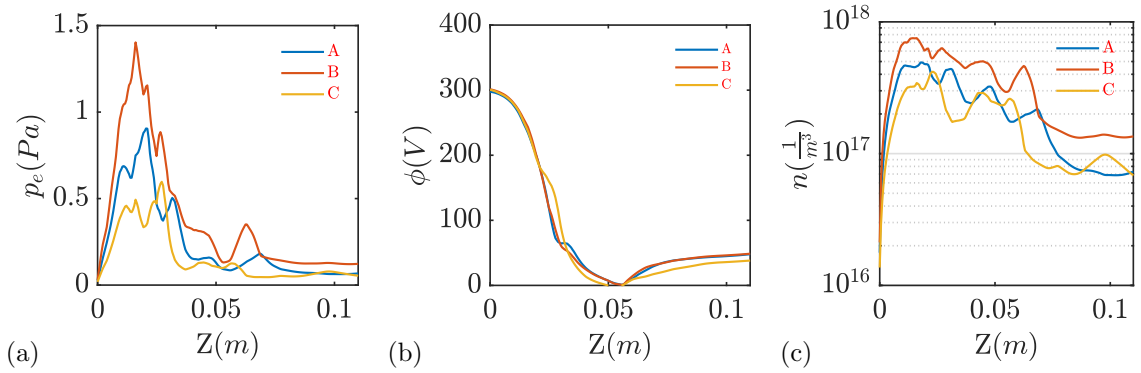

Figure 10. "Base" SPT-100 magnetic topography thruster channel center-line results for (a) electron pressure, (b) electric potential and (c) plasma density for (A) medium I_d, (B) high I_d and (C) low I_d conditions (vertical dashed line represents the channel exit)

Finally, from the performance side, some key average parameters resulting from the simulation are:

$\mathbf{I_d}$	$\mathbf{P_d}$	**Thrust**	$\mathbf{I_{sp}}$	$\eta_\mathbf{T}$	$\mathbf{P_{jet}}$	$\mathbf{P_{sheaths}}$	$\mathbf{P_{ioniz.+excit.}}$	$\mathbf{P_{cahtode}}$
$2.41A$	$723W$	$41mN$	$844s$	0.24	$168W$	$165W$	$57W$	$16W$

Table 4. Performance values for "base" SPT-100 magnetic topography

where the thrust has been obtained based on the "Lorentz force" or "Hall current force" approach described by Goebel;[23] the thrust efficiency is obtained as $\eta_T = \frac{T^2}{2\dot{m}P_d}$ and the jet power, $P_{jet} \approx \frac{T^2}{2\dot{m}}$, is obtained as in Ref. 24. The authors are aware that, while the performances are of the same order as expected, they are not in line with actual performances from this thruster, due to the non-optimized $\alpha_{anomalous}$ profile, and are only shown for reference. In a similar sense, the plasma profiles present quantities that are in the order of what is expected, but may not necessarily represent a realistic point of operation.

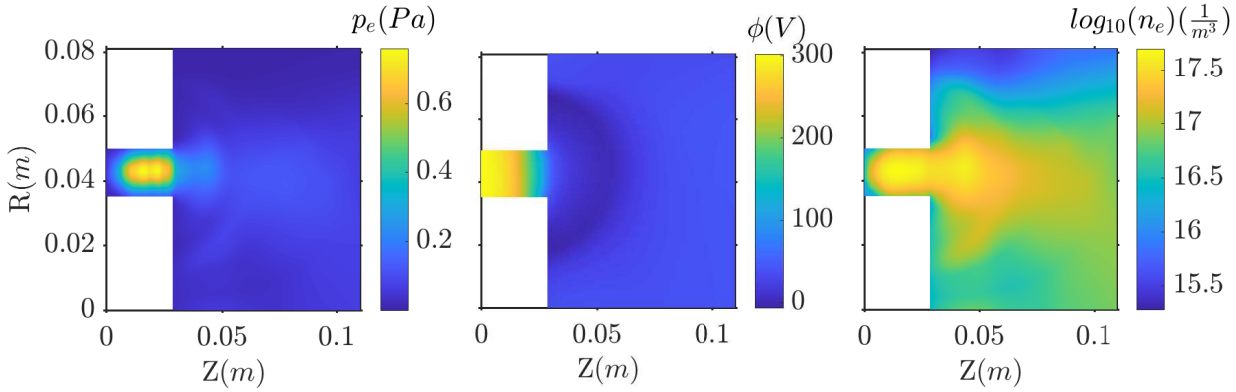

Figure 11. "Base" SPT-100 magnetic topography 2D time-averaged profiles of (a) electron pressure, (b) electric potential and (c) plasma density

B. SPT-100 singular magnetic topography

Figure 12 shows the MFAM used in the "singular" magnetic topography simulation, as well as the magnetic field in the simulation domain, where the null-magnetic-intensity point is clearly apparent. Note that the

maximum magnetic field intensity along thruster the center line ($\sim 250G$) was maintained compared to the "base" configuration, since it is an important design parameter in HETs.

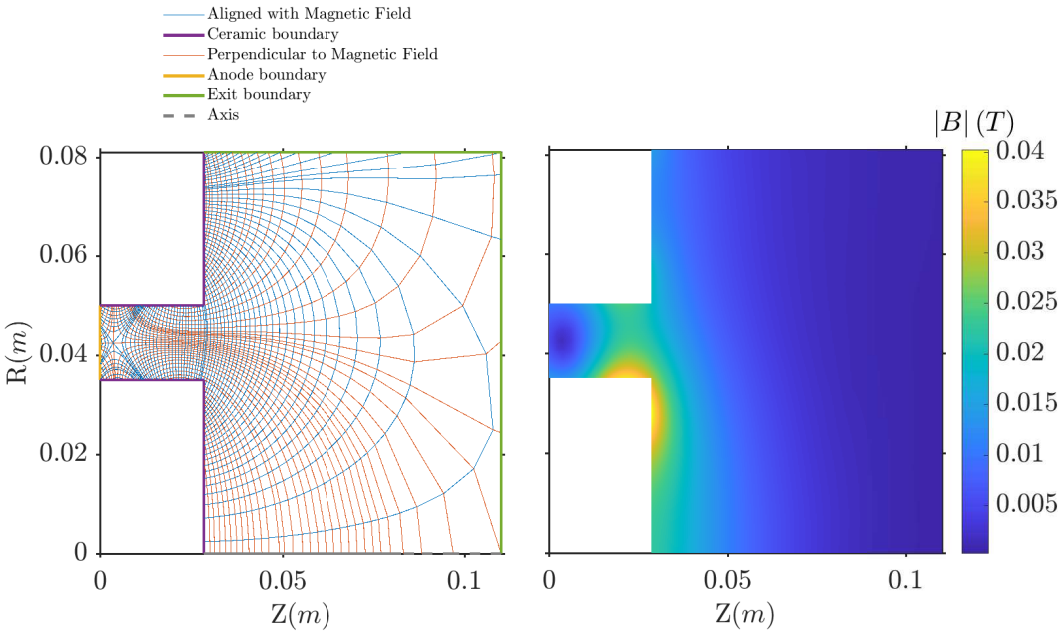

Figure 12. MFAM and Magnetic Field intensity in "singular" SPT-100 magnetic topography; (A), (B) and (C) represent, respectively, time-steps of medium, high and low discharge current

A detail of the way the MFAM treats the singular point is given in Fig. 13. Since a single node represents the singularity, faces in the mesh may still be defined in the locality of the singular point: the parallel and perpendicular directions to the magnetic field only collapse in the singular point itself; hence this region is not treated differently from the rest of the simulation domain.

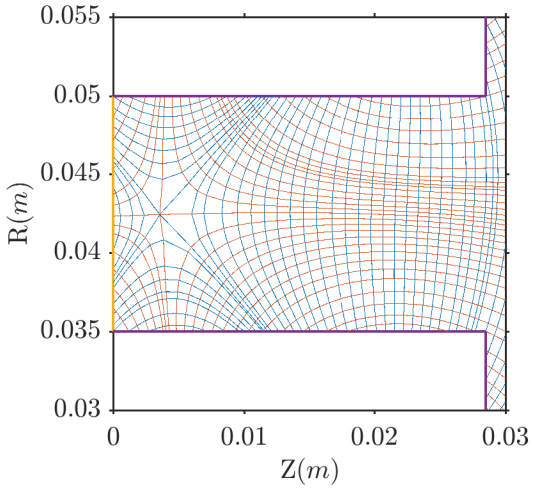

Figure 13. Channel detail for MFAM from "singular" SPT-100 magnetic topography

The inclusion of a singular point required a finer mesh than in the "base" topography, and additional lines were also included in an attempt to reduce the low quality elements next to the axis and in the downstream region of the domain; the total number of MFAM elements clearly affected the computational time in the

simulation, as may be seen in Table 5:

No. PIC mesh elements	1080
Avg. No. macroparticles	$\sim 10^5$ Neutrals, $\sim 7\times10^4$ Single Ions, $\sim 7\times10^4$ Double Ions
No. MFAM elements	2453
No. cores	20
Computation time	$18.8\times10^4 s$: $4.0\times10^3 s$ in PIC, $18.4\times10^4 s$ in NOMADS

Table 5. Simulation statistics for "singular" SPT-100 magnetic topography

Finally, simulation results and performance values are shown in Figure 14, 15, 16 in a similar fashion to Section III.A; the results are comparable since the same anomalous collisionality factor has been used in both simulations.

Table 6 shows slightly increased performances with respect to the ones for the "base" topography (Table 4). This is mirrored by the macroscopic results shown in Figures 15 and 16, where larger electron pressures and densities are achieved when compared to Figures 10 and 11; the plasma potential also presents a larger "plateau" in the near anode region.

$\mathbf{I_d}$	$\mathbf{P_d}$	**Thrust**	$\mathbf{I_{sp}}$	$\eta_\mathbf{T}$	$\mathbf{P_{jet}}$	$\mathbf{P_{sheaths}}$	$\mathbf{P_{ioniz.+excit.}}$	$\mathbf{P_{cahtode}}$
$2.94A$	$881W$	$48mN$	$980s$	0.26	$229W$	$162W$	$72W$	$10W$

Table 6. Performance values for "singular" SPT-100 magnetic topography

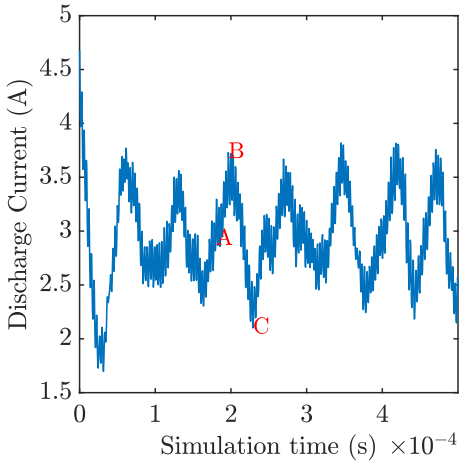

Figure 14. Discharge current in "singular" SPT-100 magnetic topography

The larger discharge current may be linked to the existence of the singular point in the anode region, which favors electron mobility; this is undoubtedly related to increased electron pressure, since the main heating term is a resistive type heating which depends on electron current, and increased electron density. In turn, these effects may be linked to increased thrust, I_{sp} and operational power, as well as the slight increase in thrust efficiency.

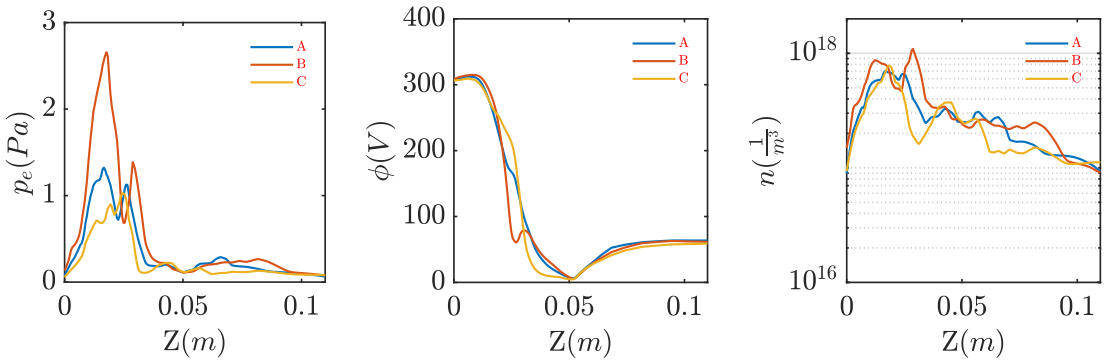

Figure 15. "Singular" SPT-100 magnetic topography thruster channel center-line results for (a) electron pressure, (b) electric potential and (c) plasma density for (A) medium I_d, (B) high I_d and (C) low I_d conditions (vertical dashed line represents the channel exit)

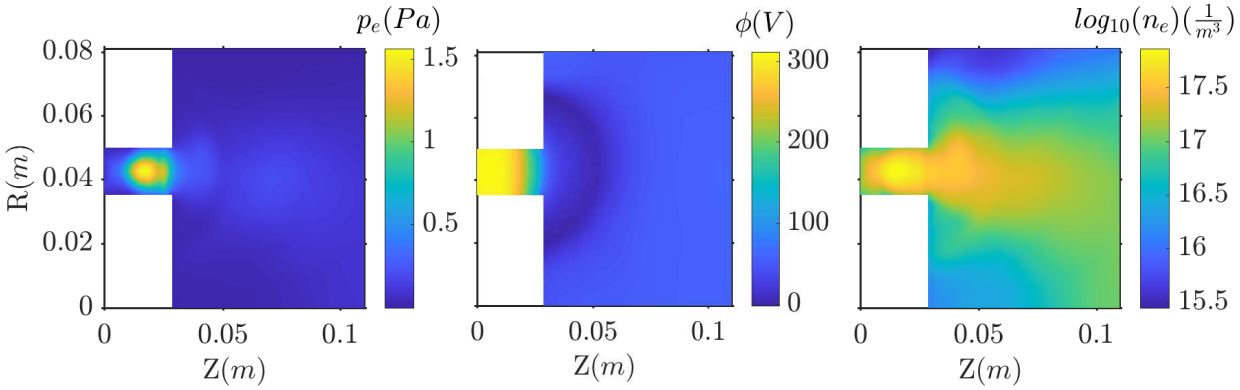

Figure 16. "Singular" SPT-100 magnetic topography 2D time-averaged profiles of (a) electron pressure, (b) electric potential and (c) plasma density

IV. Conclusions and future work

A development update on a new plasma discharge simulation platform for Hall Effect Thrusters has been provided in this manuscript. The numerical fluid model for the electron population has been commented in detail; the specifics of the heavy species Particle-In-Cell model pertaining to the simulation of thrusters, have also been provided. A comparison of Gradient Reconstruction in magnetic and cylindrical coordinates has also been shown revealing that the latter has a higher accuracy. Its implementation in the platform is ongoing and more future work will be dedicated to understanding its effects over simulation results.

Preliminary simulation results for an SPT-100 based magnetic topography, with and without a singular point within the simulation domain, have been provided to demonstrate the capabilities of the new platform in comparison to previous codes developed in the EP2 group. Future efforts will be dedicated to comparing results with other codes and experimental campaigns; in particular, the anomalous collisionality factor remains a driving force in the physical response of the plasma and its effects will be studied in detail.

Acknowledgments

This work has been partially supported by the CHEOPS project, that received funding from the European Unions Horizon 2020 research and innovation programme, under grant agreement No 730135. Additional

support came from Project ESP2016-75887, funded by the National research and development programme of Spain.

References

[1]D. Escobar and E. Ahedo. Two-dimensional electron model for a hybrid code of a two-stage Hall thruster. *IEEE Transactions on Plasma Science*, 36(5):2043–2057, 2008.

[2]J. M. Fife. *Hybrid-PIC modeling and electrostatic probe survey of Hall thrusters*. PhD thesis, Aeronautics and Astronautics Dept., Massachuchusetts Institute of Technology, Boston, September 1998.

[3]A. Domínguez, D. Pérez-Grande, P. Fajardo, and E. Ahedo. NOMADS: development of a versatile plasma discharge simulation plarform for electric propulsion. In *Space Propulsion Conference*, number 3124869, Rome, Italy, 2016.

[4]A. Domínguez, F. Cichocki, M. Merino, P. Fajrdo, and E. Ahedo. 2D and 3D hybrid PIC-fluid modelling of electric thruster plumes. In 35^{th} *International Electric Propulsion Conference*, Georgia Institute of Technology, USA, 2017. Electric Rocket Propulsion Society.

[5]M. Mitchner and C.H. Kruger Jr., editors. *Partially ionized gases*. Wiley, 1973.

[6]E.W. Bell, N. Djurić, and G.H. Dunn. Electron-impact ionization of in^+ and xe^+. *Physical Review A*, 48(6):4286, 1993.

[7]R. Santos and E. Ahedo. Implementation of the kinetic Bohm condition in a Hall thruster hybrid code. In *45th Joint Propulsion Conference, Denver, CO*, AIAA 2009-4913, 2009.

[8]E. Ahedo, R. Santos, and F. I. Parra. Fulfillment of the kinetic Bohm criterion in a quasineutral particle-in-cell model. *Physics of Plasmas*, 17(7):073507, 2010.

[9]K.U. Riemann. The Bohm criterion and sheath formation. *J. Phys. D: Appl. Phys.*, 24:492–518, 1991.

[10]K.U. Riemann. The Bohm criterion and boundary conditions for a multicomponent system. *IEEE Transactions On Plasma Science*, 23:709–716, 1995.

[11]Ioannis G Mikellides and Ira Katz. Numerical simulations of hall-effect plasma accelerators on a magnetic-field-aligned mesh. *Physical Review E*, 86(4):046703, 2012.

[12]Daniel Pérez-Grande, Oscar Gonzalez-Martinez, Pablo Fajardo, and Eduardo Ahedo. Analysis of the numerical diffusion in anisotropic mediums: Benchmarks for magnetic field aligned meshes in space propulsion simulations. *Applied Sciences*, 6(11):354, 2016.

[13]Emre Sozer, Christoph Brehm, and Cetin C Kiris. Gradient calculation methods on arbitrary polyhedral unstructured meshes for cell-centered cfd solvers. In *Proceedings of the 52nd Aerospace Sciences Meeting, National Harbor, MD, USA*, volume 1317, 2014.

[14]AR Barakat and RW Schunk. Transport equations for multicomponent anisotropic space plasmas: A review. *Plasma Physics*, 24(4):389, 1982.

[15]R.R. Hofer, I. Katz, I.G. Mikellides, D.M. Goebel, K.K. Jameson, R.M. Sullivan, and L.K. Johnson. Efficacy of electron mobility models in hybrid-pic Hall thruster simulations. *AIAA Paper*, 4924:2008, 2008.

[16]Cosmin G. Petra, Olaf Schenk, Miles Lubin, and Klaus Gärtner. An augmented incomplete factorization approach for computing the schur complement in stochastic optimization. *SIAM Journal on Scientific Computing*, 36(2):C139–C162, 2014.

[17]Cosmin G. Petra, Olaf Schenk, and Mihai Anitescu. Real-time stochastic optimization of complex energy systems on high-performance computers. *IEEE Computing in Science & Engineering*, 16(5):32–42, 2014.

[18]J. A. Bittencourt. *Fundamentals of Plasma Physics*. Springer, 2004.

[19]Makoto Hayashi. Bibliography of electron and photon cross sections with atoms and molecules published in the 20th century: Xenon. Technical report, National Inst. for Fusion Science, 2003.

[20]R.J. Goldston and P.H. Rutherford. *Introduction to Plasma Physics*. Institute of Physics Publishing, Bristol, 1995.

[21]Makoto Hayashi. Determination of electron-xenon total excitation cross-sections, from threshold to 100 ev, from experimental values of townsend's α. *Journal of Physics D: Applied Physics*, 16(4):581, 1983.

[22]E. Ahedo and V. de Pablo. Combined effects of electron partial thermalization and secondary emission in Hall thruster discharges. *Physics of Plasmas*, 14:083501, 2007.

[23]D. M. Goebel and I. Katz. *Fundamentals of electric propulsion: Ion and Hall thrusters*. Willey, New York, 2008.

[24]G.P. Sutton and O. Biblarz. *Rocket propulsion elements*. Wiley, 2010.